



Enhancing hydrogen production capability from urine-containing sewage through optimization of urea oxidation pathways



Yingzhen Zhang^{a,b}, Yonggang Lei^a, Yan Yan^{d,*}, Weilong Cai^{a,b}, Jianying Huang^{b,*}, Yuekun Lai^{a,b,*,1}, Zhiqun Lin^{c,*}

^a Qingyuan Innovation Laboratory, Quanzhou 362801, PR China

^b National Engineering Research Center of Chemical Fertilizer Catalyst (NERC-CFC), College of Chemical Engineering, Fuzhou University, Fuzhou 350116, PR China

^c Department of Chemical and Biomolecular Engineering, National University of Singapore, Singapore 117585, Singapore

^d School of Chemistry and Chemical Engineering, Anhui University of Technology, Ma'anshan 243002, PR China

ARTICLE INFO

Keywords:

Urea oxidation reaction
Fe-Ni₃S₂@NiSe₂
Selectivity
Hydrogen
Sewage

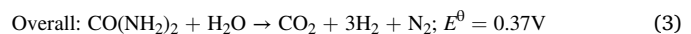
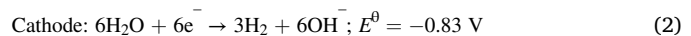
ABSTRACT

The electrochemical urea oxidation reaction (UOR) represents a promising route to sustainable hydrogen production and reuse of urea-containing sewage. However, the efficiency of UOR is hindered by the dehydrogenation of intermediate *CONH₂NH and the conversion of toxic intermediate the *CO. Herein, we report a robust strategy to elevate UOR performance by introducing iron (Fe) atoms into the Ni₃S₂@NiSe₂ heterojunctions (denoted Fe-Ni₃S₂@NiSe₂). The Fe-Ni₃S₂@NiSe₂ exhibits remarkable selectivity and electrocatalytic activity towards UOR, attributed to its reconstruction into Fe-NiOOH species during UOR process, as confirmed by *in-situ* Raman technology. Utilizing Fe-Ni₃S₂@NiSe₂ as both the cathode and anode in a single-chamber electrolytic cell, the hydrogen production rate reaches 588.4 μmol h⁻¹ in simulated urea-containing sewage and 432.1 μmol h⁻¹ in actual human urine, respectively. Notably, in both scenarios, no oxygen product is detected, and the hydrogen production efficiency surpasses that of traditional water splitting by 5.8-fold and 4.3-fold, respectively. *In-situ* infrared spectroscopy study reveals that the UOR process involves the cleavage of C-N bond and the generation of CO₂. Density functional theory calculations further signifies that the incorporation of Fe facilitates the dehydrogenation of *CONH₂NH intermediates, strengthens the *d-p* hybridization, and weakens O-H bonds, thereby resulting in reduced energy barriers for UOR. Our strategy holds promise for efficient hydrogen production from sewage via UOR, offering potential implications for wastewater treatment and clean energy generation.

1. Introduction

The limitations and environmental concerns associated with conventional fossil fuels have spurred the advancement of clean and sustainable energy sources [1,2]. Among them, hydrogen stands out as a highly promising clean energy option; however, its production is hindered by the kinetically sluggish oxygen evolution reaction (OER) during water electrolysis at the anode [3]. Notably, urea, a prevalent pollutant presents in various wastewater streams (e.g., industrial, agricultural, and municipal wastewater) [4], exhibits a significantly lower theoretical potential for urea oxidation reaction (UOR, 0.37 V) compared to OER (1.23 V) [5]. Theoretically, replacing OER with UOR and coupling the latter with hydrogen evolution reaction (HER) could

resulting in 69.9 % energy savings in hydrogen production through water electrolysis ((1.23-0.37)/1.23 = 69.9 %). The UOR coupled with HER involves two half reactions [6], represented by the following chemical reaction [7,8]:



However, the electrochemical UOR is a complex six-electron process involving the generation and desorption of multiple intermediates [9, 10], leading to unsatisfactory dynamics. Non-noble metal Ni-based chalcogenide electrocatalysts [11-13] possess distinct electronic

* Corresponding authors.

** Corresponding author at: Qingyuan Innovation Laboratory, Quanzhou 362801, PR China.

E-mail addresses: yanyan@ahut.edu.cn (Y. Yan), jyhuang@fzu.edu.cn (J. Huang), yklai@fzu.edu.cn (Y. Lai), z.lin@nus.edu.sg (Z. Lin).

¹ orcid.org/0000-0003-4100-510X

structures and stability, displaying promising electrocatalytic performance for water splitting [14,15] and oxidation reaction of various nucleophiles (e.g., urea [16], amine [17], etc.). Moreover, diverse strategies have been employed to enhance their performance, such as defect engineering and heteroatom doping or substitution, aiming at optimizing the catalyst surface's electronic structure and adsorption energy of intermediates [18–20]. Among these strategies, the doping of metal elements close to Ni [21,22] into nanostructured transition metal sulfide has proven effective in augmenting the electrochemically active surface area and electron transfer capability. Notably, a grand challenge lies in the conversion capability of the CO* intermediate during UOR process. Insufficient adsorption and desorption capability on the catalyst surface could lead to active center poisoning and reduced reaction efficiency, thereby impacting catalytic stability.

Herein, we report a facile strategy to markedly enhance hydrogen production efficiency in UOR-assisted water electrolysis by introducing Fe to promote urea decomposition. Specifically, iron-doped Ni₃S₂@NiSe₂ nanocomposites (denoted Fe-Ni₃S₂@NiSe₂) are crafted via an *in-situ* growth route and employed as self-supporting electrodes. Notably, the introduction of Fe induces morphological and electronic structure changes in Ni₃S₂@NiSe₂ heterojunctions, resulting in an expanded electrochemically active surface area and thus enhanced UOR performance and hydrogen production capacity in urea-containing wastewater. Capitalizing on Fe-Ni₃S₂@NiSe₂ nanocomposites as both cathode and the anode, hydrogen production rates of 588.4 μmol h⁻¹ and 432.1 μmol h⁻¹ are attained in 1.0 M KOH electrolyte containing 0.33 M urea and when using human urine as electrolyte, respectively. No oxygen product is detected in both electrolytes. The successful suppression of the undesired OER process in urea-containing media underscores the effectiveness of this strategy for efficient hydrogen production. Importantly, *in-situ* Raman, *in-situ* infrared spectroscopy, and density functional theory (DFT) calculations were leveraged to comprehensively elucidate the UOR mechanism, revealing that the electrocatalyst undergoes surface reconstruction during electrochemical processes and the introduction of Fe facilitates the optimization of the adsorption and desorption capabilities of key intermediates on the active centers. Our study holds significant implications for the sustainable utilization of urea-containing wastewater as a valuable resource for clean hydrogen production. As such, it contributes to the development of a more environmentally friendly and sustainable energy landscape.

2. Experimental section

2.1. Materials

Nickel(II) sulfate hexahydrate (NiSO₄·6 H₂O, AR, Aladdin), iron(III) nitrate nonahydrate (Fe(NO₃)₃·9 H₂O, 98.0 %, Damas-beta), selenium powder (Se, 99.99 %, Aladdin), thiourea (CH₄N₂S, AR, Sinopharm), N, N-dimethylformamide (DMF, AR, Sinopharm) and hydrazine hydrate (N₂H₄·H₂O, 85.0 %, Sinopharm) were utilized without any further purification. Nickel foam (NF, thickness: 2 mm) was used as self-standing electrode substrate for electrodeposition.

2.2. Material preparation

Depositing NiSe₂ on the surface of nickel foam (NF) by hydrothermal. Firstly, NF (4*6 cm²) was cleaned by 3.0 M HCl, ethanol and H₂O. Secondly, 100 mL DMF, 0.84 mL hydrazine and 3.75 mmol Se, was transfer into a 200 mL Teflon-lined stainless autoclave and heated at 180 °C for 1 h. NiSe₂ obtained was washed by water and ethanol, and vacuum dried at 60 °C.

Fe-doped Ni₃S₂ on NiSe₂ was crafted via water bath method. Immersing NiSe₂ in solution containing 160 mM NiSO₄·6 H₂O, 160 mM Fe(NO₃)₃·9 H₂O and 90 mM thiourea, and heated at 70 °C for 30 min. Washed several times with water, and vacuum dried at 60 °C to yield Fe Ni₃S₂@NiSe₂.

2.3. Characterization

The morphology of the as-prepared self-supporting electrodes were imaged using a Zeiss Sigma 300 field emission scanning electron microscope (FESEM). Transmission electron microscopy (TEM) images of electrocatalyst was taken using FEI Tecnai-G2-F20 s-twin with an accelerating voltage of 200 kV. X-ray diffraction (XRD) patterns were obtained by employing X'Pert3 Powder diffractometer with Cu K α radiation that is operated at 40 kV and 40 mA. X-ray photoelectron spectroscopy (XPS) spectra were attained by a K-Alpha+ instrument (Thermo Fisher Scientific), applying a micro-focused, monochromatic Al-K α X-ray source with 30–500 μm spot size.

2.3.1. *In-situ* Raman study

In-situ Raman study was carried out using confocal Raman microscope (DXR2xi, Thermo Fisher Scientific, 532 nm laser) under different potentials by electrochemical workstation (Versastat 3). The electrolytic cell was homemade with Teflon shell and quartz glass plate. All electrochemical tests were performed with a three-electrode configuration, where the as-synthesized Fe-Ni₃S₂@NiSe₂, Ag/AgCl electrode, and platinum wire are used as the working electrode, reference electrode, and counter electrode, respectively. The chronoamperometry curves were conducted from OCP to 1.60 V vs. RHE.

2.3.2. *In-situ* fourier transform infrared (FTIR) spectroscopy

A Perkin Elmer Spectrum 3 FTIR spectrometer equipped with a mercury cadmium telluride detector cooled with liquid nitrogen was employed for the *in-situ* FTIR study. Infrared reflection-absorption configuration was adopted. Real-time IR spectra was continuously collected by chronoamperometry from OCP to 1.6 V in 1.0 M KOH with 0.33 M urea. The spectral resolution is 8 cm⁻¹ with 44 scans per spectrum (a collection duration of 30 s).

2.4. Electrochemical measurement

All electrochemical measurements, except EIS, were performed in a three-electrode system using an electrochemical workstation (Versastat 3), where the as-synthesized self-supporting electrode, Pt plate and Hg/HgO electrode are used as the working electrode, counter electrode and reference electrode, respectively.

The Nernst equation is applied to convert potential vs. Hg/HgO electrode to potential vs. reversible hydrogen electrode (RHE):

$$E_{\text{RHE}} = E_{\text{Hg/HgO}} + 0.0059 \times \text{pH} + 0.098 \quad [23,24] \quad (4)$$

where the E_{RHE} is the potential vs. RHE and $E_{\text{Hg/HgO}}$ is the potential vs. Hg/HgO electrode. 1.0 M KOH with and without 0.33 M urea solution were used as respective electrolyte. Linear sweep voltammetry (LSV) curves were recorded from 0 to 0.8 V (vs. Hg/HgO) at a scan rate of 5 mV s⁻¹. Operando EIS was conducted over a frequency range from 10⁻² to 10⁵ Hz with AC amplitude of 10 mV by ModuLab XM electrochemical system (Solartron Analytical).

2.4.1. Faradic efficiency for UOR

The Faradic efficiency (FE) of the Fe-Ni₃S₂@NiSe₂ for UOR was calculated using the following equations [25]:

$$FE = \frac{I_{\text{UOR}}}{I} \times 100\% \quad (5)$$

$$I_{\text{UOR}} = I - I_{\text{OER}} \quad (6)$$

where, I , I_{OER} , and I_{UOR} represent the current recorded at different potential in the presence of urea, the current acquired without urea, and the current originated from urea oxidation, respectively.

2.4.2. Apparent electrochemical activation energy (E_a)

The temperature-dependent measurement was performed in a thermostatic water bath. The apparent electrochemical activation energy (E_a) for UOR can be determined by the Arrhenius equation [26]:

$$\frac{\partial(\log i_k)}{\partial(1/T)} = \frac{E_a}{2.3R} \quad (7)$$

where i_k is the kinetic current at a potential of 1.70 V (vs. RHE) at different temperatures, T is the temperature, and R is the universal gas constant. The Arrhenius plots were obtained and the E_a was extracted from the slope of the plots.

2.4.3. Product detection

To collect and analyze the emission gas during water splitting and in UOR&HER system, the gas was collected from single-chamber electrolytic cell in a continuous running. The details are as follows: (1) the air was purged with high-purity Ar gas prior to experiment. (2) in an outdoor environment, solar panel was illuminated by sunlight to generate electricity as the renewable electrical energy supply source (Video S1). (3) Gas products were detected by gas chromatography (Shimadzu GC-2014).

Supplementary material related to this article can be found online at doi:10.1016/j.apcatb.2024.124064.

2.5. DFT calculation

Density functional theory (DFT) calculations were performed by employing the generalized gradient approximation with the Perdew-Burke-Ernzerhof (PBE) functional [27], as implemented in Vienna ab initio Simulation Package (VASP) [28]. All spin-polarized calculations were performed using the projector augmented wave (PAW) pseudo-potential [29,30]. The force and energy convergence tolerance were set at 0.02 eV and 10^{-5} eV for geometry optimization, respectively. For all slab model DFT calculations, a $3 \times 3 \times 1$ Monkhorst-Pack k -point grid was used for the slab model Brillouin zone integration. Slabs were separated by 15 Å of vacuum to minimize spurious self-interactions between periodic images in the z-direction. DFT dispersion correction (DFT-D3) method was used to treat van der Waals interactions. Free energies are approximated as follows:

$$\Delta G = E_{\text{DFT}} + \Delta ZPE - T\Delta S \quad (8)$$

where E_{DFT} and ΔZPE are the total and zero-point electronic energy calculated, respectively, by DFT, and $T\Delta S$ is entropic contribution (only taken into account for gas phase species and intermediate species).

We consider the UOR process following the elementary steps as depicted in Eqs. (9)-(15):

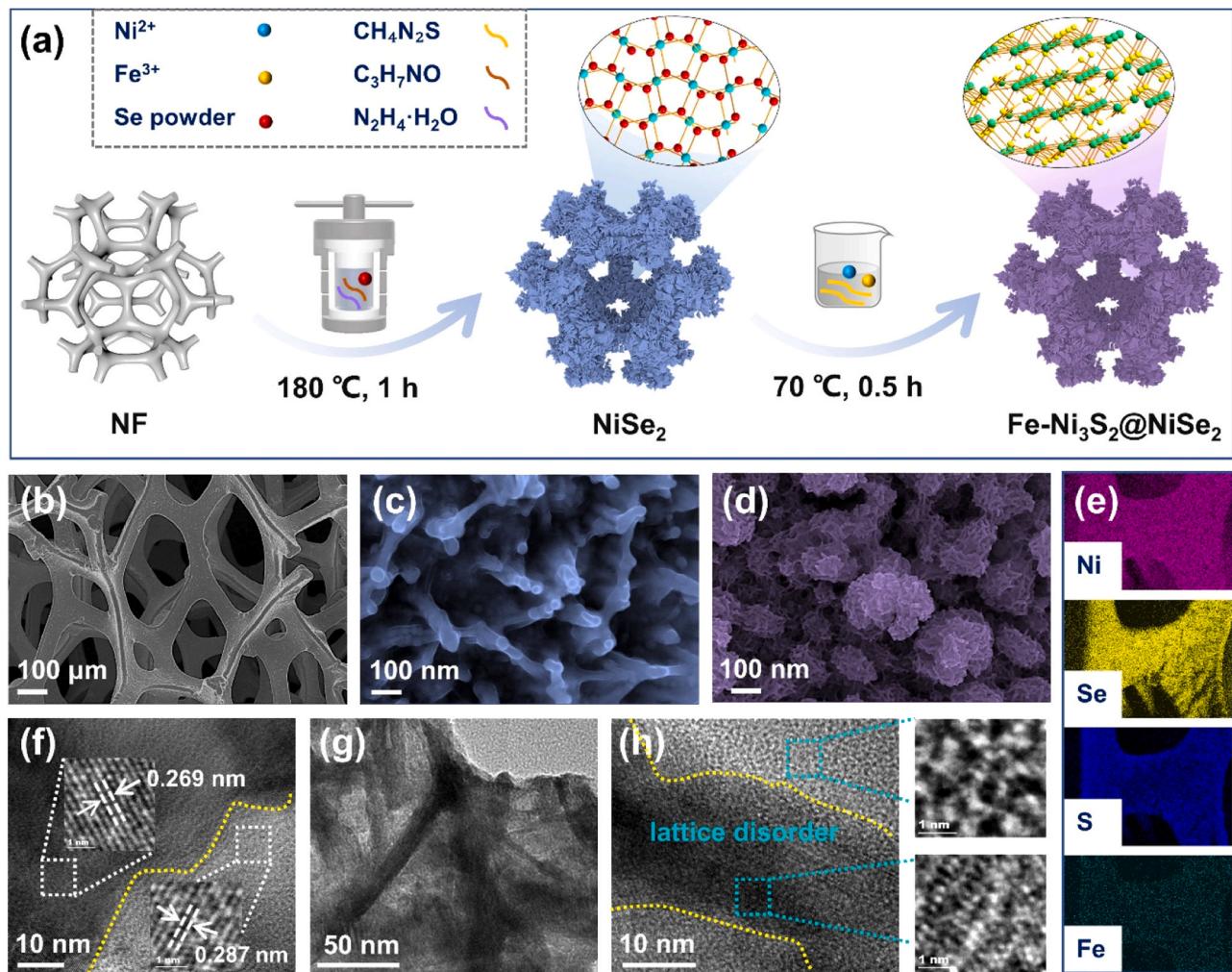
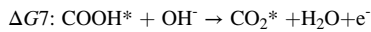
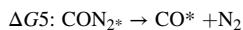


Fig. 1. (a) Schematic illustration of Fe-Ni₃S₂@NiSe₂. SEM images of (b) Nickle foam (NF), (c) NiSe₂, (d) Fe-Ni₃S₂@NiSe₂. (e) EDS-mapping of Fe-Ni₃S₂@NiSe₂. HRTEM images of (f) Ni₃S₂@NiSe₂ and (g-h) Fe-Ni₃S₂@NiSe₂, respectively.



where * represents an active site on the surface of catalyst.

3. Results and discussion

3.1. Characterizations of as-synthesized catalysts

Fig. 1a depicts the synthesis schematic of Fe-Ni₃S₂@NiSe₂ self-supporting electrocatalysts. Firstly, commercial nickel foam (NF) with a smooth surface (Fig. 1b) was used as a conductive support and Ni source. NiSe₂ was *in-situ* constructed on the surface of NF via a hydrothermal method with N,N-dimethylformamide (DMF) as the solvent and Se powder as the Se source. Subsequently, Fe-doped Ni₃S₂ was decorated on the surface of NiSe₂ via water bath heating by employing thiourea as the sulfur source, hexahydrate nickel sulfate as the nickel source, and hexahydrate iron nitrate as the iron source. Finally, Fe-Ni₃S₂@NiSe₂ nanocomposites were yielded. The SEM measurements revealed that NiSe₂ has a stalactite-like morphology (Fig. 1c), and Ni₃S₂@NiSe₂ nanocomposites display a cluster-like morphology (Figure S1), while Fe-Ni₃S₂@NiSe₂ nanocomposites display a mossy-like morphology (Fig. 1d). The energy dispersive spectroscopy (EDS) mapping shows that abundant Ni, Se and S elements were uniformly distributed on the NF substrate, with a small amount of Fe elements evenly covering the surface (Fig. 1e). The HR-TEM image shows that the Ni₃S₂@NiSe₂

heterojunction presents clear lattice fringes (Fig. 1f) with the lattice spacing of 0.269 nm and 0.287 nm, corresponding to the (210) crystal lattice of NiSe₂ [31] and the (110) crystal lattice of Ni₃S₂ [32], respectively. It is notable that the microstructure of Fe-Ni₃S₂@NiSe₂ appears more fluffy (Fig. 1g), and the lattice arrangement of Ni₃S₂@NiSe₂ becomes disordered (Fig. 1h) after the introduction of Fe elements. Such disorder may be related to the change of intrinsic electric field of Ni₃S₂@NiSe₂, which was caused by the introduction of Fe atoms [33, 34]. It will be further corroborated in the XPS study.

X-ray diffraction (XRD) was used to evaluate crystalline phase of the as-synthesized Fe-Ni₃S₂@NiSe₂ electrocatalysts. As shown in Fig. 2a, NF substrate has three Ni characteristic peaks at 2θ of 44.7°, 52.1° and 76.6°, ascribed to the (111), (200) and (220) planes, respectively (PDF No. 04-0850) [18,35]. After NiSe₂ was deposited over the NF surface, XRD peaks at 2θ of 30.2°, 33.3°, 37.1°, 50.6°, 55.7°, 58.0, 61.9° and 70.2° were observed, corresponding to the (200), (210), (211), (311), (230), (321), (400) and (420) planes of NiSe₂ (PDF No. 41-1495) [36]. Moreover, when Fe-Ni₃S₂ was deposited on the surface of NF, a set of XRD peaks at 2θ of 22.2°, 31.5°, 38.2°, 50.4° and 55.6° were found, corresponding to the characteristic peaks of (101), (110), (021), (211) and (300) crystal planes of Ni₃S₂ (PDF No. 44-1418) (Figure S2) [37]. Importantly, when Fe-Ni₃S₂ was further deposited over NiSe₂-coated NF (i.e., forming Fe-Ni₃S₂@NiSe₂), the characteristic peaks of both Fe-Ni₃S₂ and NiSe₂ can be seen, substantiating the successful preparation of Fe-Ni₃S₂@NiSe₂ electrocatalysts.

X-ray photoelectron spectroscopy (XPS) was then utilized to analyze surface chemical composition and electronic state of Fe-Ni₃S₂@NiSe₂. The Ni 2p spectrum of Fe-Ni₃S₂@NiSe₂ exhibits two main peaks at 855.40 eV (Ni²⁺ 2p_{3/2}) and 873.24 eV (Ni²⁺ 2p_{1/2}), along with two satellite peaks (Fig. 2b) [16,38]. Compared to the pure Ni₃S₂@NiSe₂, Fe doping induces a negative shift in the binding energy of the Ni 2p orbitals. This is attributed to the introduction of additional electrons by Fe

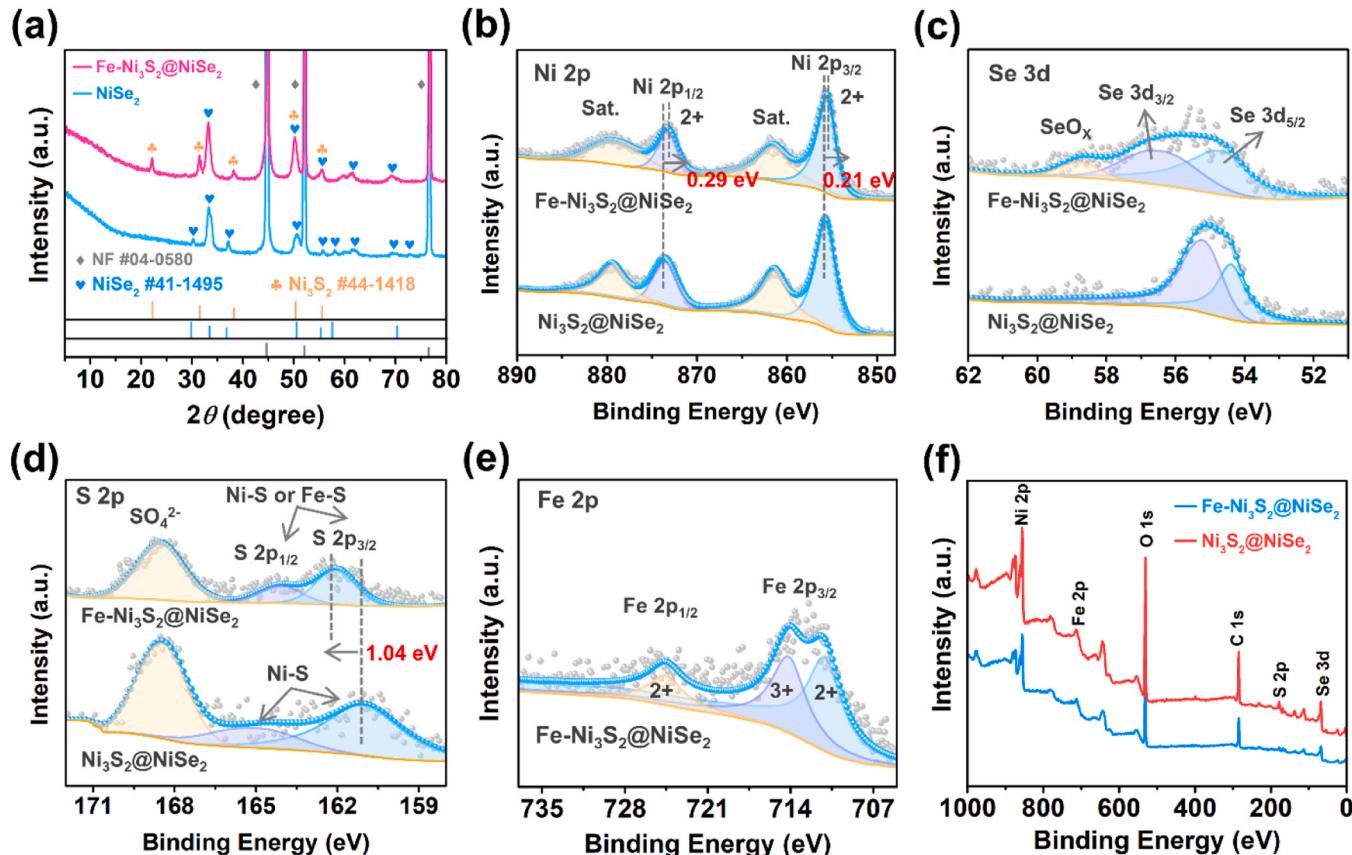


Fig. 2. (a) XRD patterns. High-resolution XPS spectra of (b) Ni 2p, (c) Se 3d, (d) S 2p and (e) Fe 2p, respectively. (f) XPS survey of Fe-Ni₃S₂@NiSe₂.

doping, thereby increasing the electron density around the Ni atoms, leading to a decrease in the binding energy of the Ni 2p orbitals. The Se 3d spectrum shows two fitted peaks at 54.62 eV and 56.40 eV, corresponding to the spin-orbits $3d_{5/2}$ and $3d_{3/2}$ of Se, respectively, and a characteristic peak ascribed to selenate was also observed at 58.75 eV (Fig. 2c) [39]. The S 2p spectrum displays two fitted peaks at 162.03 eV and 164.13 eV, assigned to the spin orbitals $3d_{3/2}$ and $3d_{1/2}$ of S 2p, respectively, which are characteristic peaks of the Ni-S bond, and the peak at 168.52 eV can be assigned to sulfate (Fig. 2d) [40]. The Fe XPS spectrum shows that the Fe 2p_{3/2} peak could be divided into two peaks centered at 711.11 eV and 714.14 eV, corresponding to Fe^{2+} and Fe^{3+} [10], respectively. The Fe 2p_{1/2} peak is located at 724.54 eV, attributing to Fe^{2+} (Fig. 2e) [40]. Fe-Ni₃S₂@NiSe₂ consists of Fe, Ni, S, Se and O elements (Fig. 2f).

3.2. Electrochemical performance characterization

The electric double layer capacitance (C_{dl}) of electrocatalysts was measured in the non-Faradaic current region (Figure S3) and used it to calculate the electrochemically active surface area (ECSA) of

electrocatalysts (Figure S4). Fig. 3a shows that Fe-Ni₃S₂@NiSe₂ has an ECSA of 192.8 cm^2 , which is larger than that of Ni₃S₂@NiSe₂ (137.8 cm^2), NiSe₂ (110.3 cm^2) and Fe-NiSe₂ (76.8 cm^2). To further investigate the number of active sites in the as-synthesized electrocatalysts, pulsed $I-t$ measurement [41] was performed by calculating the stored passing charge at 1.0 V, as shown in the cathodic $I-t$ curve (Fig. 3b). The results indicate that Fe-Ni₃S₂@NiSe₂ manifests a higher passing charge (1.55 C) compared to the pristine Ni₃S₂@NiSe₂ sample (0.63 C) under the same measurement condition, suggesting that Fe doping promotes the exposure of active sites, which is in good agreement with the ECSA results. Thus, Fe-Ni₃S₂@NiSe₂ was chosen as a representative sample to further investigate its electrocatalytic properties and reaction mechanism.

The UOR was carried out in 1.0 M KOH containing 0.33 M urea, where the competing reaction anodic OER may also take place. Linear sweep voltammetry (LSV) was initially performed to assess the electrocatalytic ability of UOR and OER for Fe-Ni₃S₂@NiSe₂. The potential difference between the UOR and OER ($\Delta E = E_{UOR} - E_{OER}$) serves as a descriptor of the electrocatalyst's selectivity. The Fe-Ni₃S₂@NiSe₂ electrocatalyst exhibits an excellent UOR selectivity ($\Delta E = 162.7 \text{ mV}$)

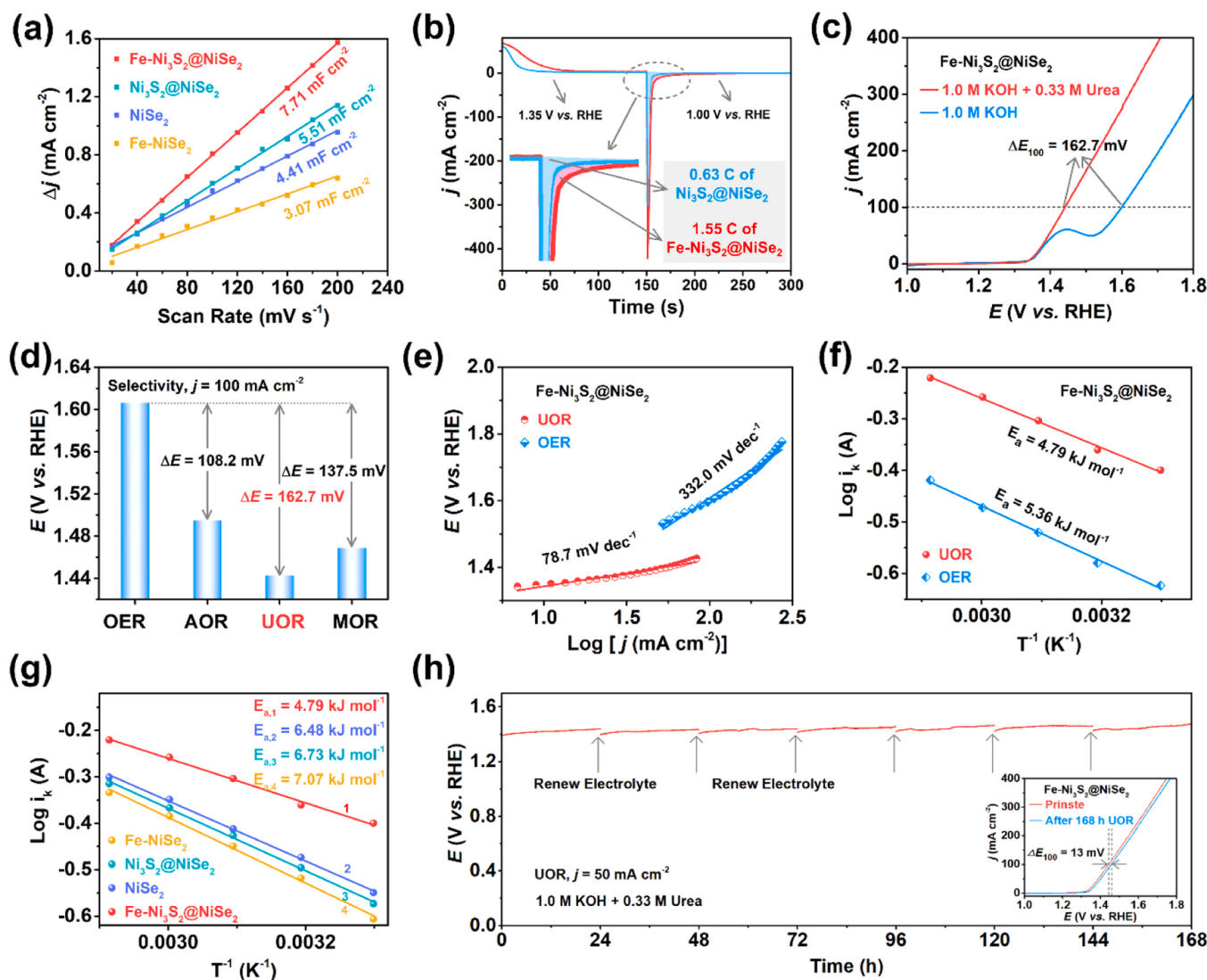


Fig. 3. (a) C_{dl} of Fe-Ni₃S₂@NiSe₂, Ni₃S₂@NiSe₂, Fe-NiSe₂, and NiSe₂. (b) Pulsed $I-t$ curves of Ni₃S₂@NiSe₂ and Fe-Ni₃S₂@NiSe₂, oxidizing the samples at 1.35 V for 150 s, followed by reduction at 1.0 V for 150 s, in 1.0 M KOH. (c) LSV curves. (d) Histogram of Fe-Ni₃S₂@NiSe₂ electrooxidation selectivity for different reactions. (e) Tafel plots of Fe-Ni₃S₂@NiSe₂ for UOR and OER, respectively. (f) Arrhenius plots infer the activation energy of Fe-Ni₃S₂@NiSe₂ for UOR and OER, respectively. (g) Arrhenius plots infer the activation energy of Fe-Ni₃S₂@NiSe₂, Ni₃S₂@NiSe₂, Fe-NiSe₂, and NiSe₂ for UOR. (h) Stability test of Fe-Ni₃S₂@NiSe₂ at $j = 50 \text{ mA cm}^{-2}$ in 1.0 M KOH with 0.33 M urea; inset shows the LSV curves of Fe-Ni₃S₂@NiSe₂ before and after the UOR stability test.

(Fig. 3c). To better reflect the intrinsic activity of the Fe-Ni₃S₂@NiSe₂, the ECSA was used to normalize the current density. The UOR exhibited excellent intrinsic activity (Figure S5). Moreover, the electrocatalyst also manifests good electrocatalytic selectivity for other small molecules (e.g., methanol as in methanol oxidation reaction (MOR) and ammonia as in ammonia oxidation reaction (AOR)) (Fig. 3d and Figure S6).

Furthermore, the onset potential (E_{onset}) reflects electrocatalytic ability of electrocatalyst. As shown in Figure S7, the E_{onset} for OER was 1.52 V in 1.0 M KOH, with a pre-oxidation peak at 1.46 V (due probably to the transition of Ni to a higher oxidation state) [20]. Upon the addition of urea, a considerable surge in the anodic current was observed, and the E_{onset} of UOR ($E_{\text{onset}} = 1.33$ V) is much lower than that of OER ($E_{\text{onset}} = 1.52$ V). Due to the slow kinetics of the OER at low potentials, the FE of the UOR was higher at low potentials compared to high potentials. Fe-Ni₃S₂@NiSe₂ exhibits a high FE, remaining close to 80 % even at an applied potential of 1.45 V vs. RHE (Figure S8). This suggests that the Fe-Ni₃S₂@NiSe₂ possesses a favorable electrocatalytic activity for urea oxidation, rendering it a promising catalyst for UOR under low potential.

Tafel plots is widely used to characterize the kinetic rate of electrocatalytic reactions, where a smaller Tafel slope indicates a more favorable catalytic reaction [42]. The smaller Tafel slope of Fe-Ni₃S₂@NiSe₂ for UOR (78.7 mV dec⁻¹) than OER (332.0 mV dec⁻¹) was observed (Fig. 3e), insinuating that the reaction kinetics of UOR is much faster than that of OER. Furthermore, the Arrhenius plot can be fitted to a straight line, with the slope representing the electrochemical activation energy (E_a) [7,43]. The E_a was tested at different temperatures (30, 40, 50, 60, and 70 °C) by LSV (Figure S9). In Fig. 3f, the E_a of Fe-Ni₃S₂@NiSe₂ was 4.79 and 5.36 kJ mol⁻¹ during UOR and OER processes, respectively. The lower E_a for UOR indicates that the energy barrier to be crossed is smaller, and the UOR proceeds faster than OER thermodynamically, which is consistent with the Tafel plot results. Additionally, during UOR process, the E_a of Fe-Ni₃S₂@NiSe₂, Ni₃S₂@NiSe₂, Fe-NiSe₂ and NiSe₂ were 4.79, 6.73, 7.07 and 6.48 kJ mol⁻¹, respectively (Fig. 3g), demonstrating that the introduction of Fe into Ni₃S₂@NiSe₂ heterostructure could effectively reduce the E_a of UOR.

The electrocatalytic stability was evaluated by chronopotentiometry. Fe-Ni₃S₂@NiSe₂ exhibited no obvious potential fluctuation at a current density of 50 mA cm⁻² during 24 h and 48 h continuous testing in 1.0 M KOH electrolyte (Figure S10), indicating that the electrocatalyst had a superb electrochemical stability. However, the potential increased significantly after 24 h in 1.0 M KOH containing 0.33 M urea. Interestingly, the potential returned to its original value after the electrolyte was replaced, suggesting that the potential increase was caused by the consumption of urea in the electrolyte. By replacing the electrolyte, the Fe-Ni₃S₂@NiSe₂ maintained an excellent electrocatalytic stability after 168 h of continuous testing for UOR (Fig. 3h), and the potential difference was only 13 mV (before and after long-time stability testing; the insert in Fig. 3h), which outperforms recently reported self-supported catalysts listed in Table S1. Furthermore, to assess the stability of Fe-Ni₃S₂@NiSe₂ under industrial conditions, the durability test was conducted at 500 mA cm⁻² (a current density consistent with industrial requirements) by chronopotentiometry. As shown in Figure S11, with increasing time, the voltage gradually increased. However, upon replacing the electrolyte with fresh solution, the current density almost entirely reverted to its initial level. This observation could be attributed to the consumption of urea (a reactant during the electrolysis process), leading to a decrease in urea concentration near the electrode and hindering mass transfer efficiency. This issue was effectively addressed by replacing the electrolyte with fresh solution. Additionally, after 5 cycles, the catalytic performance remained nearly unchanged from the initial state, demonstrating the excellent electrochemical stability of Fe-Ni₃S₂@NiSe₂.

The Fe-Ni₃S₂@NiSe₂ electrocatalyst also manifests a good HER activity in 1.0 M KOH (Figure S12), where the addition of 0.33 M urea to the electrolyte did not significantly affect the HER performance. This

signifies that the presence of urea did not hinder the HER activity and the electrocatalyst was well-suited for dual-function, single-chamber electrolyzers. To examine the performance of urea oxidation-assisted water splitting to produce hydrogen, a single-chamber electrolyzer was assembled with Fe-Ni₃S₂@NiSe₂ self-supporting electrocatalysts functioning as both the cathode and anode (Fig. 4a). To reach a current density of 100 mA cm⁻², the required voltage was 108.3 mV in 1.0 M KOH with 0.33 M urea, lower than that in 1.0 M KOH electrolyte (Figure S13). As depicted in Fig. 4b and f, in the urea oxidation-coupled with hydrogen evolution reaction (UOR||HER) system, the hydrogen production rate reached 588.4 μmol h⁻¹. In a human urine environment, the hydrogen production rate was 432.1 μmol h⁻¹. Notably, the hydrogen production rates in both aforementioned environments are higher than that in water splitting system (HER||OER; 101.8 μmol h⁻¹). Moreover, in urea-containing system, almost no oxygen (O₂) was generated, while 58.2 μmol h⁻¹ of oxygen was detected in HER||OER system (in 1.0 M KOH; Fig. 4c and Figure S14-16). It corroborates that the substitution of OER with UOR could lead to effective inhibition of O₂ generation and low-energy-consumption hydrogen production with markedly improved efficiency.

The reaction kinetics of Fe-Ni₃S₂@NiSe₂ involved in both UOR and OER processes were explored by electrochemical impedance spectroscopy (EIS). The Bode plots depict the phase angle as a function of frequency, where the low-frequency region (10⁻¹ - 10¹ Hz) is associated with interfacial reactive charge transfer processes (i.e., electrooxidation reaction of reactants, that is, urea and OH⁻ as in this study) [44,45]. As shown in Fig. 4d-e, phase angle in the low-frequency region gradually decreases with increasing potential, indicating that charge transfer of the interface reaction was accelerated, which favors the thermodynamics of water and urea oxidation reactions [46]. The phase angle value of Fe-Ni₃S₂@NiSe₂ in 1.0 M KOH with 0.33 M urea was lower than in 1.0 M KOH electrolyte, suggesting that UOR process has a faster kinetics. On the other hand, in the high-frequency region (10¹ - 10⁵ Hz), phase angle is related to electron transfer within electrocatalyst from the inner layer to surface,[44] reflecting the properties of electrocatalyst itself. In the present study, the phase angle in the high frequency region did not change significantly regardless of UOR or OER process, indicating that a fast electron transfer [47] and Fe-Ni₃S₂@NiSe₂ possesses a good electrical conductivity. During the OER process, the Nyquist plots show steep straight lines at low potentials (1.30 ~ 1.45 V vs. RHE) (Fig. 4g), which indicates an infinite charge transfer resistance. In the urea-containing system, when the applied potential exceeds 1.35 V, semi-circles are appeared in the Nyquist diagram (Fig. 4h), suggesting the occurrence of UOR and accelerated interfacial charge transfer, further confirming the faster reaction kinetics of UOR over OER.

3.3. Investigation of the catalytic mechanism

Fig. 5a depicts *in-situ* Raman investigation into the surface species of Fe-Ni₃S₂@NiSe₂ electrocatalyst during UOR process. At the open circuit potential (OCP), a characteristic peak at 1000 cm⁻¹ was observed (Fig. 5b), which can be assigned to the C-N bond in urea [48], substantiating the adsorption of urea molecules on the catalyst's surface. As the applied voltage was increased from 1.25 V to 1.30 V, two new peaks at 472 cm⁻¹ and 559 cm⁻¹ were emerged, corresponding to the Ni^{III}-O bending vibration [49] and O-Ni^{III}-O stretching vibration [50,51], respectively. This finding provide evidence that the surface of Fe-Ni₃S₂@NiSe₂ was reconstructed into Fe-NiOOH during UOR process.

After the UOR process, Fe-Ni₃S₂@NiSe₂ underwent significant morphological changes (Figure S17), suggesting that the surface of electrocatalysts was restructured during the electrochemical process. Additionally, the XRD study revealed that the crystal structure of electrocatalyst was markedly altered during UOR process, where two new characteristic peaks at 20 = 43.1° and 48.6° were seen, which can be assigned to NiOOH (Figure S18) [52]. This finding further confirms that Fe-Ni₃S₂@NiSe₂ was reconstructed during UOR process, and its

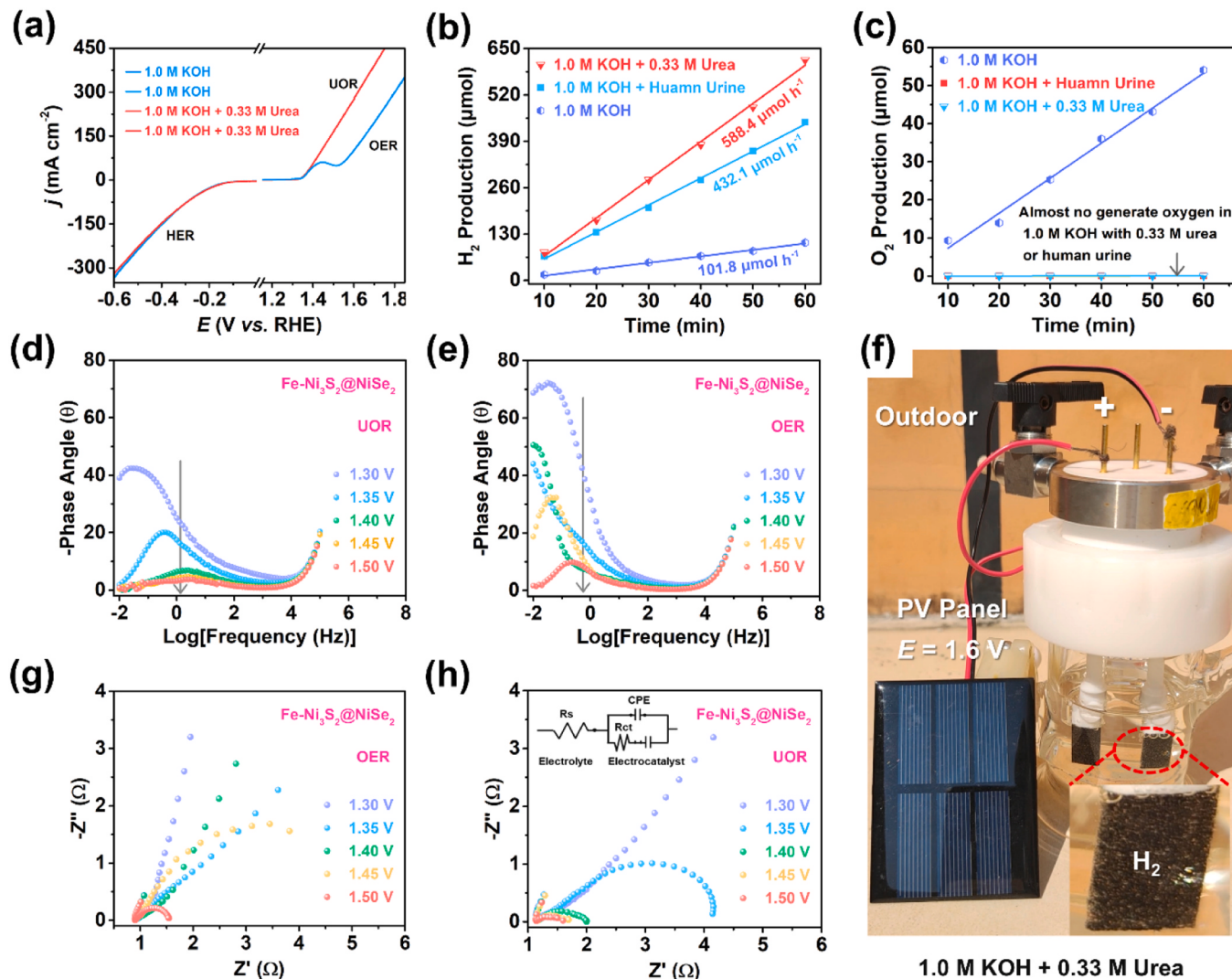


Fig. 4. Electrocatalytic performance test of $\text{Fe-Ni}_3\text{S}_2@\text{NiSe}_2$. (a) LSV curves in 1.0 M KOH with and without 0.33 M urea. (b) H_2 and (c) O_2 products at $E = 1.6 \text{ V}$ from 1.0 M KOH , 1.0 M KOH with 0.33 M urea, and 1.0 M KOH with human urine. (d-e) Bode plots of $\text{Fe-Ni}_3\text{S}_2@\text{NiSe}_2$ for (d) the UOR and (e) the OER process at various voltages. (f) Digital photograph of a two-electrode cell for the $\text{HER}||\text{UOR}$ system. (g-h) Nyquist plots of $\text{Fe-Ni}_3\text{S}_2@\text{NiSe}_2$ for (g) OER and (h) UOR process at various voltages.

morphology change was caused by this reconstruction during the electrochemical process. Furthermore, XPS spectra of $\text{Fe-Ni}_3\text{S}_2@\text{NiSe}_2$ before and after UOR process are shown in Figure S19. After UOR process, the Ni 2p spin-orbit was split into $\text{Ni } 2p_{3/2}$ and $\text{Ni } 2p_{1/2}$. The $\text{Ni } 2p_{3/2}$ peaks at 855.28 eV and 856.44 eV can be ascribed to Ni^{2+} and Ni^{3+} , while the $\text{Ni } 2p_{1/2}$ peaks at 872.96 eV and 874.86 eV can be attributed to Ni^{2+} and Ni^{3+} [53–55], respectively. In addition, the peaks at 861.19 eV and 879.22 eV correspond to the shakeup satellite peak (Figure S19 a). Compared with pristine $\text{Fe-Ni}_3\text{S}_2@\text{NiSe}_2$, Ni 2p displays a pair of peaks of Ni^{3+} , confirming the formation of NiOOH during UOR process. Furthermore, an analysis of the Fe 2p spin orbitals before and after participating in the UOR process revealed a new characteristic peak near a binding energy of 707.11 eV , corresponding to 0-valent Fe. This indicates that Fe acts as an electron acceptor, receiving electrons from Ni, facilitating the oxidation of Ni^{2+} to high-valent Ni species ($\text{Ni}^{\text{III}}\text{OOH}$) while being reduced to Fe^0 itself. These results are consistent with the XRD and *in-situ* Raman studies, substantiating that $\text{Fe-Ni}_3\text{S}_2@\text{NiSe}_2$ undergoes surface reconstruction during UOR process to form functional oxidation state of Fe-doping Ni (oxy)hydroxides (Fe-NiOOH) species, which is regarded as the active sites involved in the pathway and mechanism of UOR.

In-situ Fourier transform infrared spectroscopy (FTIR) was employed

to monitor the pivotal species during UOR process. A positive absorption peak indicates accumulation of species on the catalyst surface, whereas a negative peak suggests consumption of species on the catalyst surface [56]. For $\text{Ni}_3\text{S}_2@\text{NiSe}_2$, with an increase in the applied potential, the absorption peaks were gradually sharpened at 1270 cm^{-1} (Fig. 5d), corresponding to the $\text{C}=\text{O}$ bond in ${}^*\text{COOH}$ species (where * represents the active site). At 1640 and 2918 cm^{-1} , the bending vibration of O-H bond become stronger with the increase of applied potential, which involves the fracturing of O-H bond in ${}^*\text{COOH}$ [57]. When the applied potential is over 1.50 V , a peak at 1508 cm^{-1} was detected, which is due to the cleavage of C-N bond in ${}^*\text{O}=\text{C}-(\text{N}_2)$ species [45]. Moreover, an absorption peak owing to the stretching vibration of the N-H bond was found at 1106 cm^{-1} , which is related to urea dehydrogenation during UOR process [58]. Furthermore, the above observation also illustrates that urea preferentially undergoes the dehydrogenation process rather than breaking the C-N bond. After the applied potential is higher than 1.55 V , two peaks at 2340 and 2851 cm^{-1} associated with CO_3^{2-} were seen [59], which are attributed to the dissolution of the CO_2 product in alkaline solution [60]. In contrast, for $\text{Ni}_3\text{S}_2@\text{NiSe}_2$ without introducing Fe atoms, the bending vibration of O-H bond and the stretching vibrations of $\text{C}=\text{O}$ bond and C-N bond were weaker compared to $\text{Fe-Ni}_3\text{S}_2@\text{NiSe}_2$ (Figure S20), suggesting that the active center with iron

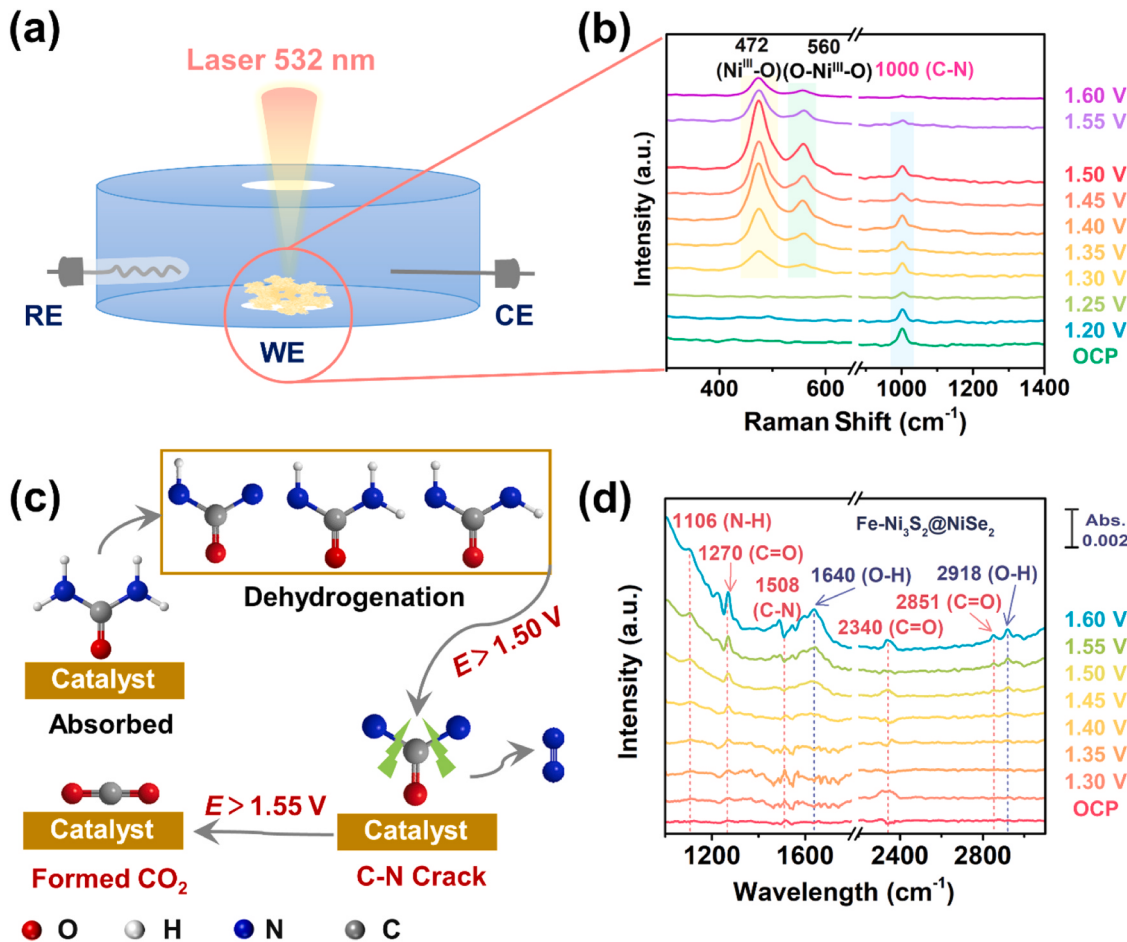


Fig. 5. (a) Schematic of *in-situ* Raman setup. (b) *In-situ* Raman spectra of $\text{Fe-Ni}_3\text{S}_2@\text{NiSe}_2$ for the UOR process. (c) Pathway of the UOR process. (d) *In-situ* FTIR spectra of $\text{Fe-Ni}_3\text{S}_2@\text{NiSe}_2$ at continuous applied potentials from OCP to 1.60 V. RE, CE, WE, and OCP represent reference electrode, counter electrode, working electrode, and open circuit potential, respectively.

introduced facilitates the oxidation of urea into the ${}^*\text{COOH}$ intermediates and thus the formation of CO_2 . On the basis of the results discussed above, a possible pathway of UOR process was proposed, involving (1) the adsorption of urea on the surface of electrocatalyst, (2) urea dehydrogenation, (3) breaking of C-N bond, and (4) formation of CO_2 , as depicted in Fig. 5c.

To decipher the origin of the superior UOR performance rendered by doping Fe atoms in $\text{Ni}_3\text{S}_2@\text{NiSe}_2$, the DFT calculation was exploited to analyze the change of energy barriers and electronic structure induced by Fe doping. Based on *in-situ* Raman, XPS and XRD results, after the UOR process, the $\text{Fe-Ni}_3\text{S}_2@\text{NiSe}_2$ heterojunction experienced surface reconstruction into high-valent $\gamma\text{-NiOOH}$, which was considered to be real active sites for UOR. Thus, $\gamma\text{-NiOOH}$ with low-index surfaces (100) was chosen as the theoretical model to represent $\text{Ni}_3\text{S}_2@\text{NiSe}_2$ (Fig. 6a). For $\text{Fe-Ni}_3\text{S}_2@\text{NiSe}_2$, the Ni sites on the surface of NiOOH was replaced by Fe atom (denoted Fe-NiOOH; Fig. 6b). The projected density of states (PDOS) of Fe-NiOOH reveals that the PDOS near the Fermi level (E_F) is mainly contributed by the Ni 3d, Fe 3d, and O 2p orbitals (Figure S21). The PDOS of NiOOH reveals that the PDOS near the Fermi energy (E_F) is mainly contributed by the Ni 3d, and O 2p orbitals (Figure S22). Notably, the anti-bonding state of Ni 3d - O 2p hybridization in Fe-NiOOH (Fig. 6c) was weaker than that of NiOOH (Figure S23), leading to a strengthened *d-p* hybridization in Fe-NiOOH, which render the possibility of enhanced electron transfer and exchange capability to activate and accelerate the UOR process. Moreover, free energy diagrams of UOR process were calculated in order to understand the intrinsic reactivity of urea dissociation at NiOOH and Fe-NiOOH surface,

respectively.

As shown in Fig. 6d, urea dissociation is proposed to consist of four steps, namely, urea adsorption (${}^*\text{CO}(\text{NH}_2)_2$), dehydrogenation (${}^*\text{CONH}_2 \rightarrow {}^*\text{CONH}_2 \rightarrow {}^*\text{CONH}$), N-N coupling (${}^*\text{CON}_2 \rightarrow \text{CO}^* + {}^*\text{N}_2$), and CO_2 desorption (${}^*\text{CO} \rightarrow {}^*\text{COOH} \rightarrow {}^*\text{CO}_2$). Specifically, the potential-determining step (PDS) of Fe-NiOOH is the CO_2 desorption with a corresponding energy barrier of 2.86 eV (Fig. 6e), which is lower than that of NiOOH (3.11 eV). Furthermore, the O-H bond in ${}^*\text{COOH}$ intermediate was found to be weaker on the Fe-NiOOH surface, as evidenced by crystal orbital Hamilton populations (COHP) analysis, further suggesting easier cleavage of the O-H bond during the PDS process. The projected COHP profiles (pCOHP) show the bonding ($\text{pCOHP} > 0$) and anti-bonding ($\text{pCOHP} < 0$) interaction of O-H bond in COOH adsorbed on Fe-NiOOH and NiOOH surface, respectively. Integrating the pCOHP to Fermi level ($E = 0$ eV) gives the ICOHP, which is a measure of bond strength [33]. Notably, COOH adsorbed on Fe-NiOOH surface exhibits a much lower ICOHP value (0.0452, in Fig. 6f) of O-H bond than that on NiOOH surface (0.0466, in Figure S24), suggesting easy cleavage of O-H bond on Fe-NiOOH. Taken together, doping Fe atom in NiOOH strengthens the *d-p* hybridization and weakens the O-H bond of PDS, thus effectively reducing the PDS of UOR process and resulting in enhanced catalytic activity.

4. Conclusion

In summary, we developed a viable strategy involving the introduction of Fe into the active site of $\text{Ni}_3\text{S}_2@\text{NiSe}_2$ heterojunction to

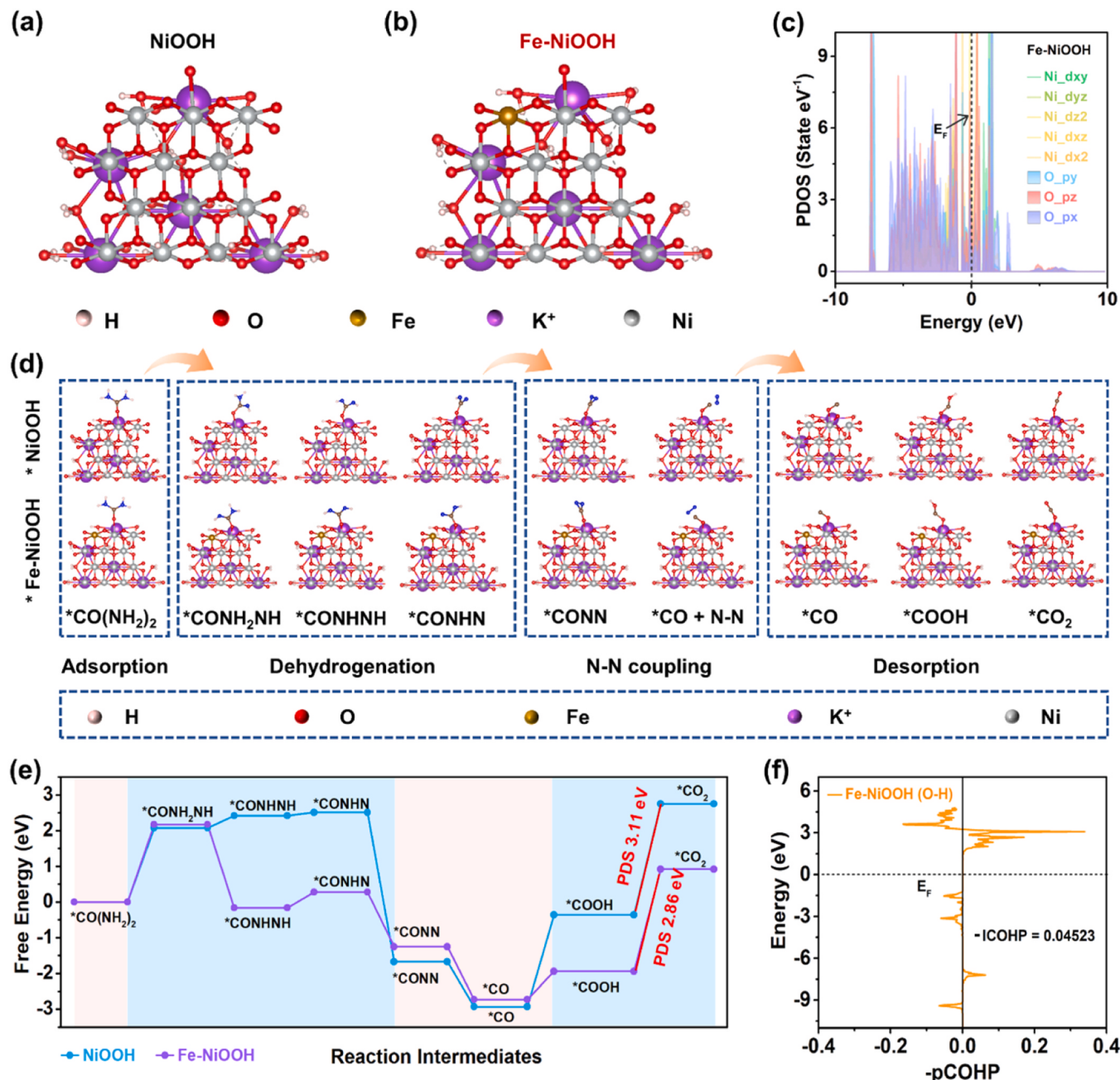


Fig. 6. Theoretical model of (a) NiOOH and (b) Fe-NiOOH, respectively. (c) PDOS of Ni 3d and O 2p orbitals in Fe-NiOOH. (d) The pathways of UOR on Fe-NiOOH and NiOOH, respectively. (e) Gibbs-free-energy of Fe-NiOOH and NiOOH towards UOR. (f) pCOHP of Fe-NiOOH for O-H interaction.

enhance the UOR-assisted HER process for the eco-friendly production of green hydrogen with low energy consumption. Importantly, as revealed by *in-situ* Raman study, the Fe-Ni₃S₂@NiSe₂ experiences surface restructuring into Fe-NiOOH species during the electrochemical process, which function as the actual catalytic center for UOR. Utilizing the as-synthesized electrocatalysts as both cathode and anode, a single-chamber electrolytic cell was constructed. The hydrogen production rates reached 588.4 $\mu\text{mol h}^{-1}$ and 432.1 $\mu\text{mol h}^{-1}$ in human urine and 1.0 M KOH containing 0.33 M urea as electrolytes, respectively, with no oxygen products detected. This observation underscores the effective suppression of the OER process in the urea-containing electrolyte, highlighting the superior selectivity of Fe-Ni₃S₂@NiSe₂ for UOR. Furthermore, DFT calculations found that the dehydrogenation of *CONH₂NH and *CONHN species occurs spontaneously, and the barrier for CO₂ generation is reduced due to the introduction of Fe. This result is

also substantiated by *in-situ* infrared spectroscopy investigation. Overall, our strategy of introducing Fe atoms into the heterojunction and substituting OER with UOR has greatly amplified the hydrogen production capacity of the electrolytic process, offering a promising solution for sewage reuse and low-energy-consumption hydrogen production.

CRediT authorship contribution statement

Yingzhen Zhang: Formal analysis, Investigation, Writing-original draft. **Yonggang Lei:** Investigation. **Yan Yan:** DFT calculation. **Weilong Cai:** Investigation. **Jianying Huang:** Conceptualization, Funding acquisition, Writing-review & editing. **Yuekun Lai:** Conceptualization, Funding acquisition, Writing-review & editing. **Zhiqun Lin:** Conceptualization, Writing-review & editing.

Declaration of Competing Interest

The authors declare that they have no known competing financial interests or personal relationships that could have appeared to influence the work reported in this paper.

Data Availability

Data will be made available on request.

Acknowledgements

The authors thank the Natural Science Foundation of Fujian Province (2022J01568), National Natural Science Foundation of China (22075046, 51972063, 21501127 and 51502185), National Key Research and Development Program of China (2022YFB3804905, 2022YFB3804900, 2019YFE0111200), Natural Science Funds for Distinguished Young Scholar of Fujian Province (2020J06038, and 111 Project (No. D17005).

Appendix A. Supporting information

Supplementary data associated with this article can be found in the online version at [doi:10.1016/j.apcatb.2024.124064](https://doi.org/10.1016/j.apcatb.2024.124064).

References

- [1] Y. Li, X.F. Wei, L.S. Chen, J.L. Shi, M.Y. He, Nickel-molybdenum nitride nanoplate electrocatalysts for concurrent electrolytic hydrogen and formate productions, *Nat. Commun.* 10 (2019) 5335.
- [2] M. Chatenet, B.G. Pollet, D.R. Dekel, F. Dionigi, J. Deseure, P. Millet, R.D. Braatz, M.Z. Bazant, M. Eikerling, I. Staffell, P. Balcombe, Y. Shao-Horn, H. Schäfer, Water electrolysis: from textbook knowledge to the latest scientific strategies and industrial developments, *Chem. Soc. Rev.* 51 (2022) 4583–4762.
- [3] Z. Zhang, X.P. Li, C. Zhong, N.Q. Zhao, Y.D. Deng, X.P. Han, W.B. Hu, Spontaneous synthesis of silver-nanoparticle-decorated transition-metal hydroxides for enhanced oxygen evolution reaction, *Angew. Chem. Int. Ed.* 59 (2020) 7245–7250.
- [4] J.N. Li, J.L. Li, T. Liu, L. Chen, Y.F. Li, H.L. Wang, X.R. Chen, M. Gong, Z.P. Liu, X. J. Yang, Deciphering and suppressing over-oxidized nitrogen in nickel-catalyzed urea electrolysis, *Angew. Chem. Int. Ed.* 60 (2021) 26656–26662.
- [5] D.C. Nguyen, T.L.L. Doan, S. Prabhakaran, D.H. Kim, N.H. Kim, J.H. Lee, Rh single atoms/clusters confined in metal sulfide/oxide nanotubes as advanced multifunctional catalysts for green and energy-saving hydrogen productions, *Appl. Catal., B* 313 (2022) 121430.
- [6] J. Zhao, Y. Zhang, H. Guo, J. Ren, H. Zhang, Y. Wu, R. Song, Defect-rich $\text{Ni(OH)}_2/\text{NiO}$ regulated by WO_3 as core-shell nanoarrays achieving energy-saving water-to-hydrogen conversion via urea electrolysis, *Chem. Eng. J.* 433 (2022) 134497.
- [7] Z.J. Ji, Y.J. Song, S.H. Zhao, Y. Li, J. Liu, W.P. Hu, Pathway manipulation via Ni, Co, and V ternary synergism to realize high efficiency for urea electrocatalytic oxidation, *ACS Catal.* 12 (2021) 569–579.
- [8] C. Huang, D. Wu, P. Qin, K. Ding, C. Pi, Q. Ruan, H. Song, B. Gao, H. Chen, P. K. Chu, Ultrafine Co nanodots embedded in N-doped carbon nanotubes grafted on hexagonal VN for highly efficient overall water splitting, *Nano Energy* 73 (2020) 104788.
- [9] L. Guo, J. Chi, J. Zhu, T. Cui, J. Lai, L. Wang, Dual-doping NiMoO_4 with multi-channel structure enable urea-assisted energy-saving H_2 production at large current density in alkaline seawater, *Appl. Catal., B* 320 (2023) 121977.
- [10] Z. Wang, W. Liu, Y. Hu, M. Guan, L. Xu, H. Li, J. Bao, H. Li, Cr-doped CoFe layered double hydroxides: Highly efficient and robust bifunctional electrocatalyst for the oxidation of water and urea, *Appl. Catal., B* 272 (2020) 118959.
- [11] D. Ma, B. Hu, W.D. Wu, X. Liu, J.T. Zai, C. Shu, T.T. Tsegaye, L.W. Chen, X.F. Qian, T.L. Liu, Highly active nanostructured CoS_2/CoS heterojunction electrocatalysts for aqueous polysulfide/iodide redox flow batteries, *Nat. Commun.* 10 (2019) 3367.
- [12] X. Tong, Y. Li, Q. Ruan, N. Pang, Y. Zhou, D. Wu, D. Xiong, S. Xu, L. Wang, P. K. Chu, Plasma engineering of basal sulfur sites on $\text{MoS}_2/\text{Ni}_3\text{S}_2$ nanorods for the alkaline hydrogen evolution reaction, *Adv. Sci.* 9 (2022) e2104774.
- [13] T. Wu, Eh Song, S.N. Zhang, M.J. Luo, C.D. Zhao, W. Zhao, J.J. Liu, F.Q. Huang, Engineering metallic heterostructure based on Ni_3N and 2M- MoS_2 for alkaline water electrolysis with industry-compatible current density and stability, *Adv. Mater.* 34 (2021) 2108505.
- [14] Y. Liu, J. Wu, K.P. Hackenberg, J. Zhang, Y.M. Wang, Y. Yang, K. Keyshar, J. Gu, T. Ogitsu, R. Vajtai, J. Lou, P.M. Ajayan, Brandon C. Wood, B.I. Yakobson, Self-optimizing, highly surface-active layered metal dichalcogenide catalysts for hydrogen evolution, *Nat. Energy* 2 (2017) 17127.
- [15] L. Yang, L. Huang, Y. Yao, L. Jiao, In-situ construction of lattice-matching $\text{NiP}_2/\text{NiSe}_2$ heterointerfaces with electron redistribution for boosting overall water splitting, *Appl. Catal., B* 282 (2021) 119584.
- [16] X.F. Lu, S.L. Zhang, W.L. Sim, S. Gao, X.W.D. Lou, Phosphorized CoNi_2S_4 yolk-shell spheres for highly efficient hydrogen production via water and urea electrolysis, *Angew. Chem. Int. Ed.* 60 (2021) 22885–22891.
- [17] Y. Huang, X. Chong, C. Liu, Y. Liang, B. Zhang, Boosting hydrogen production by anodic oxidation of primary amines over a NiSe nanorod electrode, *Angew. Chem. Int. Ed.* 57 (2018) 13163–13166.
- [18] L. Wu, F. Zhang, S. Song, M. Ning, Q. Zhu, J. Zhou, G. Gao, Z. Chen, Q. Zhou, X. Xing, T. Tong, Y. Yao, J. Bao, L. Yu, S. Chen, Z. Ren, Efficient alkaline water/seawater hydrogen evolution by a nanorod-nanoparticle-structured Ni-MoN catalyst with fast water-dissociation kinetics, *Adv. Mater.* 34 (2022) 2201774.
- [19] L. Zeng, W. Chen, Q. Zhang, S. Xu, W. Zhang, F. Lv, Q. Huang, S. Wang, K. Yin, M. Li, Y. Yang, L. Gu, S. Guo, CoSe_2 subnanometer belts with Se vacancies and Ni substitutions for the efficient electrosynthesis of high-value-added nitriles coupled with hydrogen generation, *ACS Catal.* 12 (2022) 11391–11401.
- [20] Y. Sun, H. Shin, F. Wang, B. Tian, C.W. Chiang, S. Liu, X. Li, Y. Wang, L. Tang, W. A. Goddard, M. Ding, Highly selective electrocatalytic oxidation of amines to nitriles assisted by water oxidation on metal-doped alpha-Ni(OH)_2 , *J. Am. Chem. Soc.* 144 (2022) 15185–15192.
- [21] J. Yin, J. Jin, H. Zhang, M. Lu, Y. Peng, B. Huang, P. Xi, C.H. Yan, Atomic arrangement in metal-doped NiS_2 boosts the hydrogen evolution reaction in alkaline media, *Angew. Chem. Int. Ed.* 58 (2019) 18676–18682.
- [22] Q. Sun, L. Wang, Y. Shen, M. Zhou, Y. Ma, Z. Wang, C. Zhao, Bifunctional copper-doped nickel catalysts enable energy-efficient hydrogen production via hydrazine oxidation and hydrogen evolution reduction, *ACS Sustain. Chem. Eng.* 6 (2018) 12746–12754.
- [23] J. Yin, J. Jin, H. Liu, B. Huang, M. Lu, J. Li, H. Liu, H. Zhang, Y. Peng, P. Xi, C. H. Yan, NiCo_2O_4 -based nanosheets with uniform 4 nm mesopores for excellent Zn-air battery performance, *Adv. Mater.* 32 (2020) 2001651.
- [24] P. Liu, B. Chen, C.W. Liang, W.T. Yao, Y.Z. Cui, S.Y. Hu, P.C. Zou, H. Zhang, H. J. Fan, C. Yang, Tip-enhanced electric field: a new mechanism promoting mass transfer in oxygen evolution reactions, *Adv. Mater.* 33 (2021) 2007377.
- [25] Z. Ma, H. Wang, H. Ma, S. Zhan, Q. Zhou, Three-dimensional crystalline- $\text{Ni}_5\text{P}_4@$ amorphous- NiO_x core-shell nanosheets as bifunctional electrode for urea electro-oxidation and hydrogen evolution, *Fuel* 315 (2022) 123279.
- [26] Q. Wen, Y. Lin, Y. Yang, R. Gao, N. Ouyang, D. Ding, Y. Liu, T. Zhai, In situ chalcogen leaching manipulates reactant interface toward efficient amine electrooxidation, *ACS Nano* 16 (2022) 9572–9582.
- [27] J.P. Perdew, K. Burke, M. Ernzerhof, Generalized gradient approximation made simple, *Phys. Rev. Lett.* 78 (1997), 1396–1399.
- [28] G. Kresse, J. Hafner, Ab initio molecular dynamics for liquid metals, *Phys. Rev. B* 47 (1993) 558–561.
- [29] G. Kresse, D. Joubert, From ultrasoft pseudopotentials to the projector augmented-wave method, *Phys. Rev. B* 59 (1999) 1758–1775.
- [30] S. Grimme, J. Antony, S. Ehrlich, H. Krieg, A consistent and accurate ab initio parametrization of density functional dispersion correction (DFT-D) for the 94 elements H–Pu, *J. Chem. Phys.* 132 (2010) 154104.
- [31] J.Y. Xue, F.L. Li, B. Chen, H. Geng, W. Zhang, W.Y. Xu, H. Gu, P. Braunschtein, J. P. Lang, Engineering multiphasic $\text{MoSe}_2/\text{NiSe}$ heterostructure interfaces for superior hydrogen production electrocatalysis, *Appl. Catal., B* 312 (2022) 121434.
- [32] K. Tao, Y. Gong, J. Lin, Epitaxial grown self-supporting $\text{NiSe}/\text{Ni}_3\text{S}_2/\text{Ni}_{12}\text{P}_5$ vertical nanofiber arrays on Ni foam for high performance supercapacitor: Matched exposed facets and re-distribution of electron density, *Nano Energy* 55 (2019) 65–81.
- [33] H. Qin, Y. Ye, J. Li, W. Jia, S. Zheng, X. Cao, G. Lin, L. Jiao, Synergistic engineering of doping and vacancy in Ni(OH)_2 to boost urea electrooxidation, *Adv. Funct. Mater.* 33 (2023) 2209698.
- [34] Y. Cheng, H. Guo, L. Zhang, M. Wang, J. Zhou, T. Qian, C. Yan, Mo-mediated transition of the lattice to long-range disorder enables ultra-high current density hydrogen production at low potentials, *Adv. Funct. Mater.* 33 (2023) 2208718.
- [35] M.A. Ahsan, A.R. Puente Santiago, Y. Hong, N. Zhang, M. Cano, E. Rodriguez-Castellon, L. Echegoyen, S.T. Sreenivasan, J.C. Noveron, Tuning of tri-functional NiCu bimetallic nanoparticles confined in a porous carbon network with surface composition and local structural distortions for the electrocatalytic oxygen reduction, oxygen and hydrogen evolution reactions, *J. Am. Chem. Soc.* 142 (2020) 14688–14701.
- [36] Z. Liu, C.Z. Zhang, H. Liu, L.G. Feng, Efficient synergism of NiSe_2 nanoparticle/ NiO nanosheet for energy-relevant water and urea electrocatalysis, *Appl. Catal., B* 276 (2020) 119165.
- [37] J. Hu, S. Zhu, Y. Liang, S. Wu, Z. Li, S. Luo, Z. Cui, Self-supported $\text{Ni}_3\text{Se}_2@\text{NiFe}$ layered double hydroxide bifunctional electrocatalyst for overall water splitting, *J. Colloid Interf. Sci.* 587 (2021) 79–89.
- [38] G. Liu, M. Wang, Y. Wu, N. Li, F. Zhao, Q. Zhao, J. Li, 3D porous network heterostructure $\text{NiCe}@\text{NiFe}$ electrocatalyst for efficient oxygen evolution reaction at large current densities, *Appl. Catal., B* 260 (2020) 118199.
- [39] K. Li, J. Zhang, R. Wu, Y. Yu, B. Zhang, Anchoring CoO domains on CoSe_2 nanobelts as bifunctional electrocatalysts for overall water splitting in neutral media, *Adv. Sci.* 3 (2016) 1500426.
- [40] X. Chen, Q. Wang, Y. Cheng, H. Xing, J. Li, X. Zhu, L. Ma, Y. Li, D. Liu, S-doping triggers redox reactivities of both iron and lattice oxygen in FeOOH for low-cost and high-performance water oxidation, *Adv. Funct. Mater.* 32 (2022) 2112674.
- [41] Z. Li, X. Li, H. Zhou, Y. Xu, S.M. Xu, Y. Ren, Y. Yan, J. Yang, K. Ji, L. Li, M. Xu, M. Shao, X. Kong, X. Sun, H. Duan, Electrocatalytic synthesis of adipic acid coupled with H_2 production enhanced by a ligand modification strategy, *Nat. Commun.* 13 (2022) 5009.
- [42] C.X. Chen, S.Q. He, K. Dastafkan, Z. Zou, Q. Wang, C. Zhao, Sea urchin-like NiMoO_4 nanorod arrays as highly efficient bifunctional catalysts for

electrocatalytic/photovoltage-driven urea electrolysis, *Chin. J. Catal.* 43 (2022) 1267–1276.

[43] W. Wang, Y. Wang, R. Yang, Q. Wen, Y. Liu, Z. Jiang, H. Li, T. Zhai, Vacancy-rich Ni(OH)_2 drives the electrooxidation of amino C–N bonds to nitrile C–N bonds, *Angew. Chem. Int. Ed.* 59 (2020) 16974–16981.

[44] Y.X. Lu, T.Y. Liu, C.L. Dong, C.M. Yang, L. Zhou, Y.C. Huang, Y.F. Li, B. Zhou, Y. Q. Zou, S.Y. Wang, Tailoring competitive adsorption sites by oxygen-vacancy on cobalt oxides to enhance the electrooxidation of biomass, *Adv. Mater.* 34 (2021) 2107185.

[45] W. Chen, L.T. Xu, X.R. Zhu, Y.C. Huang, W. Zhou, D.D. Wang, Y.Y. Zhou, S.Q. Du, Q.L. Li, C. Xie, L. Tao, C.L. Dong, J.L. Liu, Y.Y. Wang, R. Chen, H. Su, C. Chen, Y. Q. Zou, Y.F. Li, Q.H. Liu, S.Y. Wang, Unveiling the electrooxidation of urea: intramolecular coupling of the N–N bond, *Angew. Chem. Int. Ed.* 60 (2021) 7297–7307.

[46] K.Z. Gu, D.D. Wang, C. Xie, T.H. Wang, G. Huang, Y.B. Liu, Y.Q. Zou, L. Tao, S. Y. Wang, Defect-rich high-entropy oxide nanosheets for efficient 5-hydroxymethylfurfural electrooxidation, *Angew. Chem. Int. Ed.* 60 (2021) 20253–20258.

[47] W. Chen, B.B. Wu, Y.Y. Wang, W. Zhou, Y.Y. Li, T.Y. Liu, C. Xie, L.T. Xu, S.Q. Du, M.L. Song, D.D. Wang, Y.B. Liu, Y.F. Li, J.L. Liu, Y.Q. Zou, R. Chen, C. Chen, J. Y. Zheng, Y. Li, J. Chen, S.Y. Wang, Deciphering the alternating synergy between interlayer Pt single-atom and NiFe layered double hydroxide for overall water splitting, *Energy Environ. Sci.* 14 (2021) 6428–6440.

[48] X. Zheng, J. Yang, P. Li, Z. Jiang, P. Zhu, Q. Wang, J. Wu, E. Zhang, W. Sun, S. Dou, D. Wang, Y. Li, Dual-atom support boosts nickel-catalyzed urea electrooxidation, *Angew. Chem. Int. Ed.* 62 (2023) e202217449.

[49] Y. Liao, Y. Chen, L. Li, S. Luo, Y. Qing, C. Tian, H. Xu, J. Zhang, Y. Wu, Ultrafine homologous $\text{Ni}_2\text{P}-\text{Co}_2\text{P}$ heterostructures via space-confined topological transformation for superior urea electrolysis, *Adv. Funct. Mater.* 33 (2023) 2303300.

[50] M. Cai, Q. Zhu, X. Wang, Z. Shao, L. Yao, H. Zeng, X. Wu, J. Chen, K. Huang, S. Feng, Formation and stabilization of NiOOH by introducing alpha- FeOOH in LDH: composite electrocatalyst for oxygen evolution and urea oxidation reactions, *Adv. Mater.* 35 (2023) 2209338.

[51] L. Fan, Y. Ji, G. Wang, J. Chen, K. Chen, X. Liu, Z. Wen, High entropy alloy electrocatalytic electrode toward alkaline glycerol valorization coupling with acidic hydrogen production, *J. Am. Chem. Soc.* 144 (2022) 7224–7235.

[52] R. Wang, C. Xu, J.M. Lee, High performance asymmetric supercapacitors: New NiOOH nanosheet/graphene hydrogels and pure graphene hydrogels, *Nano Energy* 19 (2016) 210–221.

[53] L. Wang, Y. Zhu, Y. Wen, S. Li, C. Cui, F. Ni, Y. Liu, H. Lin, Y. Li, H. Peng, B. Zhang, Regulating the local charge distribution of Ni active sites for the urea oxidation reaction, *Angew. Chem. Int. Ed.* 60 (2021) 10577–10582.

[54] M. Cai, Q. Zhu, X. Wang, Z. Shao, L. Yao, H. Zeng, X. Wu, J. Chen, K. Huang, S. Feng, Formation and stabilization of NiOOH by introducing alpha- FeOOH in LDH: composite electrocatalyst for oxygen evolution and urea oxidation reactions, *Adv. Mater.* 35 (2023) e2209338.

[55] X. Cao, P. Wen, R. Ma, Y. Liu, S. Sun, Q. Ma, P. Zhang, Y. Qiu, Ni_2P nanocrystals modification on $\text{Ta}:\alpha\text{-Fe}_2\text{O}_3$ photoanode for efficient photoelectrochemical water splitting: In situ formation and synergistic catalysis of $\text{Ni}_2\text{P}@\text{NiOOH}$ cocatalyst, *Chem. Eng. J.* 449 (2022) 137792.

[56] H. Yu, S. Zhu, Y. Hao, Y.M. Chang, L. Li, J. Ma, H.Y. Chen, M. Shao, S. Peng, Modulating local interfacial bonding environment of heterostructures for energy-saving hydrogen production at high current densities, *Adv. Funct. Mater.* 33 (2023) 2212811.

[57] W.K. Han, J.X. Wei, K. Xiao, T. Ouyang, X. Peng, S. Zhao, Z.Q. Liu, Activating lattice oxygen in layered lithium oxides through cation vacancies for enhanced urea electrolysis, *Angew. Chem. Int. Ed.* 61 (2022) e202206050.

[58] J. Wang, F. Mo, J. Fei, W. Ling, M. Cui, H. Lei, L. Jiang, Y. Huang, Insights into the synergistic effect between nickel and molybdenum for catalyzing urea electrooxidation, *Carbon Neutral* 1 (2022) 267–276.

[59] K. Zhang, C. Liu, N. Graham, G. Zhang, W. Yu, Modulation of dual centers on cobalt-molybdenum oxides featuring synergistic effect of intermediate activation and radical mediator for electrocatalytic urea splitting, *Nano Energy* 87 (2021) 106217.

[60] L. Wang, S. Zhu, N. Marinkovic, S. Kattel, M. Shao, B. Yang, J.G. Chen, Insight into the synergistic effect between nickel and tungsten carbide for catalyzing urea electrooxidation in alkaline electrolyte, *Appl. Catal. B* 232 (2018) 365–370.